Three-dimensional reconstruction of shape and piecewise constant region values for optical tomography using spherical harmonic parametrization and a boundary element method

Athanasios D Zacharopoulos[1], **Simon R Arridge**[1], **Oliver Dorn**[2], **Ville Kolehmainen**[3] **and Jan Sikora**[4]

[1] Department of Computer Science, University College London, Gower St, London, WC1E 6BT, UK
[2] Departamento de Matemáticas, Universidad Carlos III de Madrid, Avda de la Universidad, 30, 28911 Leganés, Madrid, Spain
[3] Department of Physics, University of Kuopio, PO Box 1627, FIN-70211 Kuopio, Finland
[4] Warsaw University of Technology, Institute of the Theory of Electrical Engineering, Measurement and Information Systems, Koszykowa 75, 00-661 Warsaw, Poland

E-mail: A.Zacharopoulos@cs.ucl.ac.uk

Abstract

We consider the recovery of smooth 3D region boundaries with piecewise constant coefficients in optical tomography. The method is based on a parametrization of the closed boundaries of the regions by spherical harmonic coefficients, and a Newton type optimization process. A boundary integral formulation is used for the forward modelling. The calculation of the Jacobian is based on an adjoint scheme for calculating the corresponding shape derivatives. We show reconstructions for 3D situations. In addition we show the extension of the method for cases where the constant optical coefficients are also unknown. An advantage of the proposed method is the implicit regularization effect arising from the reduced dimensionality of the inverse problem.

M This article features online multimedia enhancements

(Some figures in this article are in colour only in the electronic version)

1. Introduction

1.1. Optical tomography

In this paper, we explore a technique for the retrieval of the internal boundaries of 3D regions in frequency domain optical tomography (OT) [4], which seeks the recovery of optical properties such as light absorption and scattering, given measurements of transmitted light through biological tissue of several centimetres in thickness. The optical parameter values $\{\mu_a, \mu_s'\}$, where μ_a is the absorption coefficient and μ_s' the (reduced) scattering coefficient, are assumed to be piecewise constant in the three-dimensional bounded domain Ω with jumps at the interior interfaces. There are several physiologically interesting observations which can be derived from the knowledge of the absorption and scattering coefficients of light in tissue. This includes tissue oxygenation, blood volume and blood oxygenation [23, 55]. Primary applications are the detection and classification of tumourous tissue in the breast, monitoring of the oxygenation level in infant brain tissue and functional brain activation studies.

Our model for light propagation in biological tissue is the diffusion equation

$$-\nabla \cdot D(\mathbf{r})\nabla \Phi(\mathbf{r}; \omega) + \mu_a(\mathbf{r})\Phi(\mathbf{r}; \omega) + \frac{\mathrm{i}\omega}{c}\Phi(\mathbf{r}) = s(\mathbf{r}; \omega), \qquad (1)$$

where $\Phi(\mathbf{r}; \omega)$ is the photon density, c is the speed of light in the medium and $s(\mathbf{r}; \omega)$ describes the source term. It represents the number of photons per unit volume at the source position $\mathbf{r}$; ω is the modulation frequency. The diffusion coefficient is given by

$$D = \frac{1}{3(\mu_a + \mu_s')}. \qquad (2)$$

In the remainder of the paper we refer to the problem parameters in terms of $\{\mu_a, D\}$ for convenience. The appropriate boundary condition is of the Robin type

$$\Phi(\mathbf{r}; \omega) + 2\alpha D(\mathbf{r})\frac{\partial \Phi(\mathbf{r}; \omega)}{\partial \nu} = 0, \qquad \mathbf{r} \in \partial\Omega, \qquad (3)$$

where α models the refractive index difference at the boundary $\partial\Omega$.

A commonly used approach in problems of this type is to discretize the unknown functions $\{\mu_a, D\}$ into a finite-dimensional space spanned by local basis functions of voxels or other small 3D volume elements [45]. Then, the goal is to search this space so as to optimize the fit of a numerical model of (1) and (3) (such as a finite difference or finite elements) to measured data. The main difficulties which arise in this situation are as follows: (1) the geometry of biological tissue is complicated and the construction of a volume element discretization is cumbersome; (2) a model with sufficient resolution introduces a large number of parameters and therefore increases the size of the search space for the inverse problem; (3) the ill-posed nature of the problem together with the noisy data requires for additional regularization techniques to be incorporated into the reconstruction.

1.2. The shape-based approach

In this paper we propose an alternative shape-based reconstruction method that works with parametric representations of 3D shapes for overcoming the above-mentioned difficulties. This approach assumes that the distribution of the optical parameters inside the body Ω is arranged into L disjoint regions Ω_ℓ

$$\Omega = \bigcup_{\ell=1}^{L} \Omega_\ell, \qquad (4)$$

which are separated by smooth closed interfaces Γ_ℓ, and have piecewise constant optical properties $\{\mu_{a,\ell}, D_\ell\}$. Then, we may describe the propagation of light (1), (3) by a set of coupled Helmholtz equations

$$-\nabla^2 \Phi_\ell + k_\ell^2 \Phi_\ell = q_\ell \quad \text{in } \Omega_\ell, \tag{5}$$

where $q_\ell = \frac{s}{D_\ell}$, and with boundary conditions

$$\Phi_{\ell+1} = \Phi_\ell, \qquad D_{\ell+1} \frac{\partial \Phi_{\ell+1}}{\partial \nu} = D_\ell \frac{\partial \Phi_\ell}{\partial \nu} \quad \text{on } \Gamma_\ell, \tag{6}$$

$$\Phi_1 + 2\alpha D_1 \frac{\partial \Phi_1}{\partial \nu} = 0 \quad \text{on } \partial\Omega. \tag{7}$$

The respective (complex) wavenumbers are

$$k_\ell^2(\omega) = \frac{\mu_{a,\ell} + \frac{i\omega}{c}}{D_\ell}. \tag{8}$$

We use a boundary integral formulation so that the discretization of the volume of the domain Ω will be replaced by that of the interfaces Γ_ℓ separating the disjoint regions that comprise Ω. Moreover, the shapes and locations of these interfaces are described by finite sets of shape coefficients $\{\gamma_\ell\}$. The forward problem uses a boundary element method (BEM) to discretize the mapping from these shape coefficients $\{\gamma_\ell\}$ and the (piecewise constant) optical parameter values $\{\mu_{a,\ell}, D_\ell\}$ inside the individual subregions to the data $\mathbf{g}$ collected on the surface $\partial\Omega$. The inverse problem is then to find the representation $\{\gamma_\ell\}$ and the values $\{\mu_{a,\ell}, D_\ell\}$ from the measurements $\mathbf{g}$. A crucial element in solving this inverse problem is the determination of shape sensitivities or shape derivatives, which is done here using an adjoint field technique [9, 44]. Once these quantities have been calculated, a Jacobian matrix can be constructed from them which will then be used as a component of a classical output least-squares Gauss–Newton optimization scheme with line-search globalization.

The shape representation employed in our work is based on spherical harmonics, which allows reasonably complex shapes to be represented with relatively few parameters. By representing a parametric surface as an (x, y, z) triple in which each coordinate is expanded independently in a spherical harmonic series, the method is not limited to star-shaped objects. Moreover, an attractive feature of this technique is the fact that the dimension of the search space for the inverse problem is much smaller than for classical voxel-based techniques. This potentially leads to a less ill-posed inverse problem. Furthermore, the construction of a BEM discretization using surface meshes is typically less costly than constructing volume meshes for voxel-based techniques.

An approach related to that presented in this paper can be found in [30, 31]. In that work, 2D shapes and piecewise constant coefficients for light absorption and diffusion in OT are recovered using a Fourier series representation of the closed region boundaries and a finite element method for solving the forward model. Moreover, a local mesh refinement is used during the procedure of the shape estimation. These results have only been implemented in 2D but are also promising for 3D situations.

Another approach to the optical tomography problem using shape recovery is presented in [29]. In that paper inhomogeneities in the absorption parameter are approximated by an ellipsoidal shape. Discretization of a slab domain into voxels was used and the location and ellipsoidal shape of objects with absorbing contrast was recovered.

Boundary elements have been used in numerous applications of structural optimization. In [10], an application of the forward solution for the obstacle recovery problem for 3D acoustics and traction free cavities in an elastic medium is handled with the use of BEM. The

parametrization suggested for the unknown boundaries is based on an ellipsoidal, defined by nine geometric parameters: the three centroid coordinates, the three principal axes and three Euler angles for the rotation. Our approach slightly generalizes this idea and allows for more freedom for specifying the complexity of the involved shapes.

An additional aspect that we consider in this paper is the combination of the search for the unknown interfaces with the simultaneous reconstruction of the piecewise constant domain optical parameters $\{\mu_{a,\ell}, D_\ell\}$. This topic is related to the asymptotic techniques for the reconstruction of small objects such as those developed by [13] for the diffusion parameter and [5] for the absorption parameter. In these works attention is drawn to the ambiguity or 'cross-talk' in the recovery of both shape and contrast. The numerical results presented in this paper are consistent with these findings and are discussed in more detail in section 5.

We also mention the related work presented in [24]. In that approach, small geometric inclusions are nucleated inside an acoustic medium using a topological derivative, and the question of simultaneous determination of the acoustic parameters (density) inside these nucleated objects is addressed.

Other related shape-based work in the literature includes the application of shape reconstruction techniques in electrical impedance tomography (EIT) as, for example, reported in [19, 20, 42], in heat transfer problems as reported in [1, 36, 38], in acoustic problems as reported in [32] and in potential problems as reported in [26]. Shape reconstruction techniques based on level sets for diffuse optical tomography are presented in [16, 17, 46]. Level set techniques for shape reconstruction in other applications (including, e.g., inverse electromagnetic scattering, inverse acoustic scattering and EIT) are reported, for example, in [12, 14, 15, 22, 21, 28, 33, 34, 41, 43, 44, 51].

In [52, 53], the shape of a 3D perfectly conducting object is reconstructed from electromagnetic measurements using spherical harmonics as radial basis functions. A technique for detecting small electromagnetic inclusions by a MUSIC type algorithm is presented in [3]. A more comprehensive list of shape-based inverse problems and possible reconstruction techniques can be found in the two recent review papers [18, 39] and in the various further references given there.

The remainder of the paper is organized as follows. In section 2, we discuss the parametric representation of the 3D shapes, and we describe the forward and the shape-based inverse problem for OT. In section 3 we derive an adjoint formulation of the shape derivative. Section 4 describes practical issues of the implementation of the forward problem using a BEM. In section 5 we present and discuss numerical results, and in section 6 we give conclusions.

2. Formulation of the problem

2.1. Parametric representation of surfaces

Our main interest lies in the use of geometric prior information in order to create a sufficiently realistic model of the different subregions of an anatomical structure. Keeping in mind applications in head and brain imaging, we decided to use the head geometry as a test bed. We can use good resolution MRI or CT-scan images as prototypes (figure 1). Both imaging modalities use voxel maps to create an image. One key component of the surface representation is the choice to use a harmonic mapping of the surface net onto the sphere's surface, which is made possible by the specific representation of each Cartesian component by spherical harmonics as described in the following.
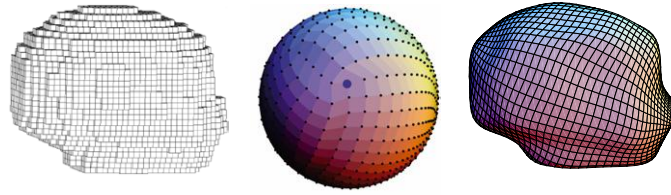
Figure 1. Segmented MRI data of a baby's scalp and as voxel volume (left). The mapping of the surface on the sphere (middle). The parametric representation with 11 degrees of spherical harmonics (right).

The surface locations $\mathbf{r}|_\Gamma$ are given by the representation

$$\mathbf{r}|_\Gamma = \begin{cases} x_\Gamma(\vartheta, \varphi) = \sum_{l=0}^{W} \sum_{m=-l}^{l} C_{l,x}^m Y_l^m(\vartheta, \varphi), \\ y_\Gamma(\vartheta, \varphi) = \sum_{l=0}^{W} \sum_{m=-l}^{l} C_{l,y}^m Y_l^m(\vartheta, \varphi), \\ z_\Gamma(\vartheta, \varphi) = \sum_{l=0}^{W} \sum_{m=-l}^{l} C_{l,z}^m Y_l^m(\vartheta, \varphi), \end{cases} \tag{9}$$

with expansion coefficients $\{C_l^m\}$. Here, the basis functions $Y_l^m(\vartheta, \varphi)$ are the well-known (complex-valued) spherical harmonic functions, and W is the maximum degree of spherical harmonics that we used for the particular representation. In particular, the zeroth degree coefficients

$$\mathbf{c} = \begin{pmatrix} C_{0,x}^0 \\ C_{0,y}^0 \\ C_{0,z}^0 \end{pmatrix} \tag{10}$$

are representative of the position for the centre of the object. In general, the higher order basis functions are roughly assumed to represent more detailed characteristics of the surface, whereas the lower order ones describe more the overall features such as volume, orientation etc. As a technical point, since surfaces are defined in real Euclidean space $\mathbb{R}^3$, we define a basis of real functions as

$$\tilde{Y}_l^m(\vartheta, \varphi) := \begin{cases} \mathrm{Re}\big[Y_l^m\big](\vartheta, \varphi), & \text{when } m \leqslant 0, \\ \mathrm{Im}\big[Y_l^m\big](\vartheta, \varphi), & \text{when } m > 0, \end{cases} \tag{11}$$

for which the orthogonal condition

$$\int_{S^2} \tilde{Y}_l^m \tilde{Y}_{l'}^{m'} \mathrm{d}S = \delta_{mm'} \delta_{ll'}$$

still holds. For simplicity we introduce the notation

$$\gamma = \{\gamma_k\} = \big\{ C_{l,x}^m, C_{l,y}^m, C_{l,z}^m \big\}, \qquad \text{with} \quad l = 1, \ldots, W, m = -l, \ldots, l \tag{12}$$

such that the new index k ranges over $k = 1, \ldots, 3W^2$. $\{\gamma_k\}$ describes the finite set of spherical harmonic coefficients for the surface Γ up to degree W.

We mention here that the mapping $\mathbf{r}_\Gamma(\vartheta, \varphi)$ of the unit sphere on the surface also provides a convenient mechanism for producing a reliable quality mesh of the surface as required for the boundary element method. Starting from an embedded icosahedron and by tessellation a regular triangular mesh was created on the sphere's surface and was then constituently mapped upon the parametric surface using the functional (9). Using this mapping, any regular mesh $\mathbb{V}$ which is defined on the sphere surface can easily be mapped to any parametrically defined object.
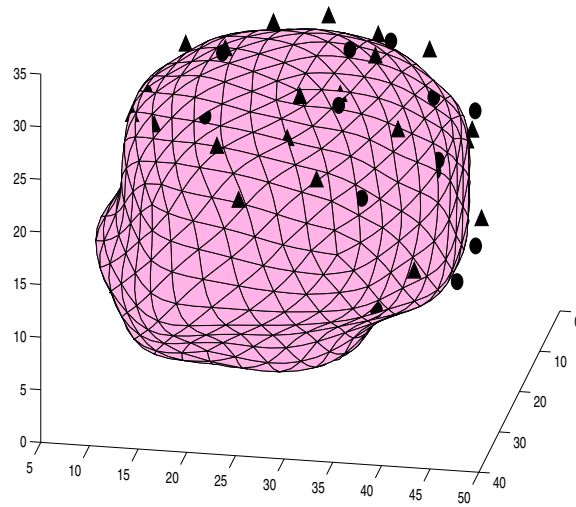
Figure 2. The experimental setup used in our OT experiments, shown from the back; by circles we denote the sources $q^{(j)}$ and by triangles the detectors $m^{(i)}$.

2.2. The forward problem

Let us denote the space of fields Φ_1 in region Ω_1 by F, and the space of measurements $\mathbf{g}$ by Z. The space of parameter functions $\{\mu_a, D\}$ will be denoted by P. The data $\mathbf{g}$ are calculated by a *linear measurement operator* $\mathcal{M} : F \to Z$ in the form

$$\mathbf{g} = \mathcal{M}\Phi_1. \tag{13}$$

This operator typically calculates a vector of weighted integrals of the (complex-valued) fields Φ along a set of surface elements at $\partial\Omega$ where the detectors are located (one surface integral per detector), with detector-specific weight functions. We denote the set of these weighting functions by

$$\mathbb{W} = \{w_i(\mathbf{r})\}, \quad \mathbf{r} \text{ on } \partial\Omega, i = 1, \dots, M. \tag{14}$$

For our analysis, it is sufficient to assume that this operator is linear and its *adjoint measurement operator* $\mathcal{M}^* : Z \to F$ is well defined. It will be used later for defining artificial 'adjoint sources' at the receiver locations for calculating shape sensitivities. We will demonstrate in section 4 how these operators are modelled in our numerical experiments. Note that the data $\mathbf{g}$ will depend on the frequency ω used in the experiment, on the source location and on the parameter distribution $\{\mu_a, D\}$. The set of source locations and frequencies will be our design parameters for the experimental setup. In the following we will for simplicity assume that only one frequency ω is chosen and fixed, even though the method can be generalized in a straightforward way to a multiple-frequency setup.

As in conventional pixel-based reconstruction we assume multiple sources $q^{(j)}$, $j = 1, \dots, S$ and detectors $m^{(i)}$, $i = 1, \dots M$, located at the surface $\partial\Omega$ (see figure 2). During the experiment, light is emitted from one source at a time and the photons leaving the domain are collected at all the detectors. We denote by $g_{j,i}$ the measurements which correspond to detector i and source j. The combined measurements for a source j are denoted by $\mathbf{g}^{(j)}$. Combining furthermore the measurements $\mathbf{g}^{(j)}$ for all of our chosen sources gives rise to a stacked measurement vector $\mathbf{g}$.
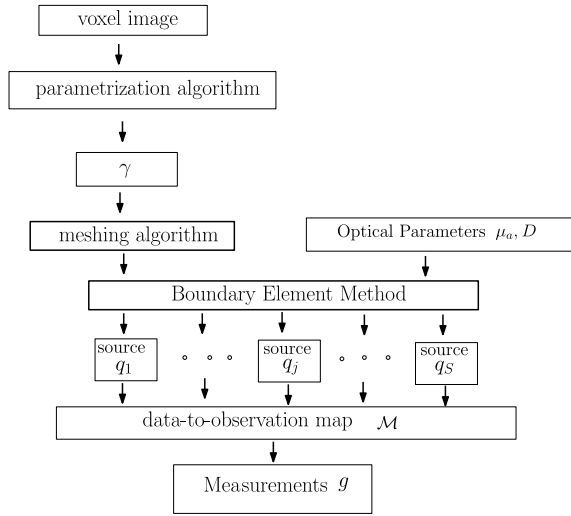
Figure 3. Schematic view of the forward model.

We can then define the nonlinear forward operator $\mathcal{K}(\gamma, \mu_{\mathrm{a}}, D) = \mathcal{M}\Phi_1$ as the mapping from the optical properties $D = \{D_\ell\}_{\ell=1,\ldots,L}$ and $\mu_a = \{\mu_{\mathrm{a},\ell}\}_{\ell=1,\ldots,L}$ of the individual regions $\Omega_\ell, \ell = 1, \ldots, L$, and the geometric parameters $\gamma = \{\gamma_\ell\}_{\ell=1,\ldots,L}$ to the measurements on the surface of Ω. Combining the measurements from the S independent sources, the forward mapping takes the form

$$\mathbf{g} = \begin{pmatrix} \mathbf{g}^{(1)} \\ \mathbf{g}^{(j)} \\ \vdots \\ \mathbf{g}^{(S)} \end{pmatrix} = \begin{pmatrix} \mathcal{K}_1(\gamma, \mu_{\mathrm{a}}, D) \\ \mathcal{K}_2(\gamma, \mu_{\mathrm{a}}, D) \\ \vdots \\ \mathcal{K}_S(\gamma, \mu_{\mathrm{a}}, D) \end{pmatrix} = \mathcal{K}(\gamma, \mu_{\mathrm{a}}, D). \tag{15}$$

A schematic view of our forward model is shown in figure 3.

2.3. The inverse problem

The most general inverse problem to be considered in our framework would be the simultaneous reconstruction of shape parameters γ and optical parameters μ_{a} and D from the data $\mathbf{g}$. However, in most practical applications which we have in mind, good estimates for the optical parameters $\mu_{\mathrm{a},\ell}$ and D_ℓ in most of the regions Ω_ℓ are available, and only those optical parameters which correspond to unknown anomalies need to be recovered. Therefore in this paper we consider the boundary shape $\partial\Omega$ and optical parameters $\mu_{\mathrm{a},1}$, D_1 of the outer region as known and only look for the shape parameters and the optical coefficients of an unknown embedded anomaly described by the interior regions.

It will be convenient to split the formal derivation of our reconstruction scheme into the part for recovery of the shape parameters and the part for recovery of the optical parameters, which will be implemented in an alternating fashion as explained in section 5.3. In the following we concentrate on the technique for calculating shape sensitivities by an adjoint scheme which only requires the evaluation of forward and adjoint fields at the interfaces between subregions, which are readily available in a boundary element method framework.
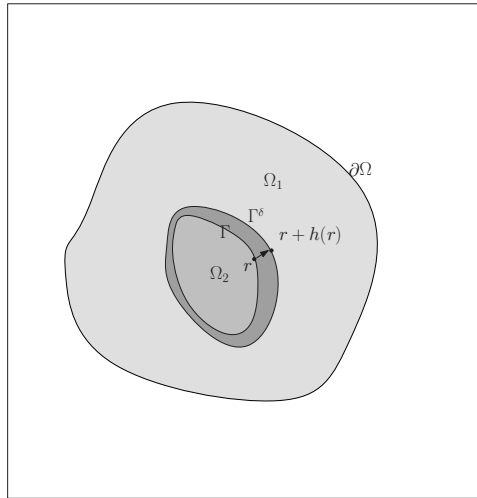
Figure 4. The perturbed boundary Γ^δ used for the calculation of the Fréchet derivative.

Starting from a geometric configuration defined by the initial set of shape coefficients $\gamma^{(0)}$, we will try to search for the set $\hat\gamma$ that minimizes the distance between computed $\mathcal{K}(\gamma, \mu_a, D)$ and measured data $\mathbf{g}$. For this purpose, we define the least-squares functional

$$\Xi(\gamma) = \|\mathbf{g} - \mathcal{K}(\gamma, \mu_a, D)\|^2. \tag{16}$$

We solve the inverse problem by a cost minimization procedure:

$$\text{find } \hat\gamma \text{ so that } \Xi(\hat\gamma) = \min_\gamma \|\mathbf{g} - \mathcal{K}(\gamma, \mu_a, D)\|^2. \tag{17}$$

A typical way to minimize such a cost function is a Newton-type method [8, 54], where we search for a minimum for $\Xi(\gamma)$ by iterations of local linearization and Taylor expansion around the current estimate $\gamma^{(n)}$ as

$$\gamma^{(n+1)} = \gamma^{(n)} + \left(\mathsf{J}_n^T \mathsf{J}_n + \Lambda\right)^{-1} \mathsf{J}_n^T (\mathbf{g} - \mathcal{K}(\gamma^{(n)}, \mu_a, D)). \tag{18}$$

In (18), the Jacobian matrix J is a derivative of the forward operator $\mathcal{K}$ with respect to the shape coefficients γ,

$$\mathsf{J} = \frac{\partial \mathcal{K}(\gamma, \mu_a, D)}{\partial \gamma}, \tag{19}$$

and Λ is a Levenberg–Marquandt control term [35]. In our implementation, we take Λ to be a constant times the identity.

The modified Newton method (18) for the minimization of the residual (16) produces the descent direction in the parameter space by providing a step $\delta\gamma^{(n)} = \gamma^{(n+1)} - \gamma^{(n)}$. In practice, a quadratic fit line search method [40] is introduced in order to globalize the optimization.

3. Fréchet derivative

In order to determine the descent direction for the cost functional $\Xi(\gamma)$ we need to calculate its derivatives with respect to the shape parameters γ. For this purpose we need to calculate the Fréchet derivative (or shape derivative) of the data with respect to the current shape. We will discuss in the following the simplified case of two subregions (see figure 4). The extension to the case of more than two subregions is straightforward.

3.1. Linearization

Consider the perturbed interface

$$\Gamma \to \Gamma + \Gamma^\delta,$$

between our two subregions Ω_1 and Ω_2. The perturbation is described by a vector *displacement field*

$$\mathbf{r} \to \mathbf{r} + \mathbf{h}(\mathbf{r}) \quad \text{for } \mathbf{r} \text{ on a neighborhood of } \Gamma.$$

In our application the interface Γ as well as the perturbation vector field $\mathbf{h}$ is composed by using spherical harmonics. This means, we have $\Gamma = \Gamma(\gamma)$ with γ defined by (12), and $\Gamma + \Gamma^\delta = (\Gamma + \Gamma^\delta)(\gamma + \delta\gamma)$ with $\delta\gamma$ being a perturbation. However, the following derivation of shape sensitivities will be done for the case of more general shape perturbations Γ^δ. We denote the difference between calculated data $\mathcal{M}\Phi_1(\Gamma)$, corresponding to the interface Γ, and the physically measured data $\mathbf{g}$ by a nonlinear operator

$$\mathcal{R}(\Gamma) = \mathcal{M}\Phi_1(\Gamma) - \mathbf{g}, \tag{20}$$

which also depends on the optical parameters μ_a and D and the source position and frequency, all of them being assumed fixed for the following derivation. The linearized form is denoted by $\mathcal{R}'(\Gamma)$. In the following we want to derive expressions for this linearized operator $\mathcal{R}'(\Gamma)$ and its adjoint $\mathcal{R}'^*(\Gamma)$. The Jacobian J in (19) can then be calculated from this expression by applying the chain rule with $\Gamma = \Gamma(\gamma)$. Practically, this amounts to a projection onto the chosen set of basis functions. As shown formally in [18], these projections are performed by calculating weighted surface integrals of the surface sensitivities (as derived here) over the interfaces between the individual subregions, the weights being given by the corresponding spherical harmonic functions. For more details see [18].

Since the internal geometry is altered, so are the fields, and we have

$$\Phi_\ell \to \Phi_\ell + \Phi_\ell^\delta$$

for $\ell = 1, 2$. Making use of results from [25], we have that Φ_ℓ^δ satisfy

$$\nabla^2 \Phi_1^\delta - k_1^2 \Phi_1^\delta = 0 \quad \text{in } \Omega_1, \tag{21}$$

$$\nabla^2 \Phi_2^\delta - k_2^2 \Phi_2^\delta = 0 \quad \text{in } \Omega_2, \tag{22}$$

with boundary and interface conditions

$$\Phi_1^\delta - \Phi_2^\delta = -h_{\hat{\nu}} \left(\frac{\partial \Phi_1}{\partial \nu} - \frac{\partial \Phi_2}{\partial \nu} \right) \quad \text{on } \Gamma, \tag{23}$$

$$D_1 \frac{\partial \Phi_1^\delta}{\partial \nu} - D_2 \frac{\partial \Phi_2^\delta}{\partial \nu} = -h_{\hat{\nu}} \left(D_1 k_1^2 - D_2 k_2^2 \right) \Phi + \nabla_\parallel \cdot [h_{\hat{\nu}} (D_1 \nabla_\parallel \Phi_1 - D_2 \nabla_\parallel \Phi_2)] \quad \text{on } \Gamma, \tag{24}$$

$$\Phi_1^\delta + 2\alpha D_1 \frac{\partial \Phi_1^\delta}{\partial \nu} = 0 \quad \text{on } \partial\Omega, \tag{25}$$

where we introduced the notation $h_{\hat{\nu}} = (\mathbf{h} \cdot \hat{\nu})$ for the normal component of the displacement. The data are perturbed to

$$\mathbf{g} \to \mathbf{g} + \mathbf{g}^\delta.$$

In the above and in the remainder of the text we use the following notation. The quantities $\hat{\nu}_\ell, \ell = 1, 2$, denote the outward pointing normal directions with respect to the domains

Ω_ℓ, $\ell = 1, 2$, respectively. Along Γ we define furthermore $\hat{v} = \hat{v}_2 = -\hat{v}_1$. Accordingly, we will have along Γ the relation $\frac{\partial}{\partial \nu} = \frac{\partial}{\partial \nu_2} = -\frac{\partial}{\partial \nu_1}$. At the outer boundary $\partial\Omega$ we have $\hat{v} = \hat{v}_1$.

3.2. Adjoint formulation

Since expressions (21)–(25) only depend on $h_{\hat{v}}$ at Γ, this will be our quantity of interest for developing an adjoint formulation. Let ζ be an arbitrary element of the data space Z, and denote, as defined earlier, the parameter space by P and the space of photon density functions inside Ω_1 by F. We use canonical L_2-spaces for all quantities considered here. We consider the relation between the inner products

$$\langle \mathcal{R}'(\Gamma)h_{\hat{v}}, \zeta \rangle_Z = \langle h_{\hat{v}}, \mathcal{R}'^*(\Gamma)\zeta \rangle_P. \tag{26}$$

From Green's theorem, we have for any fields Ψ_1 and Ψ_2

$$\int_{\Omega_1} D_1 \overline{\Psi}_1 \left(\nabla^2 \Phi_1^\delta - k_1^2 \Phi_1^\delta \right) d\mathbf{r} + \int_{\Omega_2} D_2 \overline{\Psi}_2 \left(\nabla^2 \Phi_2^\delta - k_2^2 \Phi_2^\delta \right) d\mathbf{r} + \left\langle \mathcal{M}\Phi_1^\delta, \zeta \right\rangle_Z$$

$$= \int_{\Omega_1} D_1 \Phi_1^\delta \left(\nabla^2 \overline{\Psi}_1 - k_1^2 \overline{\Psi}_1 \right) d\mathbf{r} + \int_{\Omega_2} D_2 \Phi_2^\delta \left(\nabla^2 \overline{\Psi}_2 - k_2^2 \overline{\Psi}_2 \right) d\mathbf{r}$$

$$+ \int_{\Gamma \cup \partial\Omega} \left(\overline{\Psi}_1 D_1 \frac{\partial \Phi_1^\delta}{\partial \nu_1} - \Phi_1^\delta D_1 \frac{\partial \overline{\Psi}_1}{\partial \nu_1} \right) dS + \int_{\Gamma} \left(\overline{\Psi}_2 D_2 \frac{\partial \Phi_2^\delta}{\partial \nu_2} - \Phi_2^\delta D_2 \frac{\partial \overline{\Psi}_2}{\partial \nu_2} \right) dS$$

$$+ \left\langle \Phi_1^\delta, \mathcal{M}^*\zeta \right\rangle_F, \tag{27}$$

where we have used that $\partial\Omega_2 = \Gamma$ and $\partial\Omega_1 = \Gamma \cup \partial\Omega$. We now choose Ψ_1 and Ψ_2 to be solutions of the following *adjoint equations*

$$\nabla^2 \Psi_1 - \overline{k_1^2} \Psi_1 = -\frac{1}{D_1} \mathcal{M}^*\zeta \quad \text{in } \Omega_1, \tag{28}$$

$$\nabla^2 \Psi_2 - \overline{k_2^2} \Psi_2 = 0 \quad \text{in } \Omega_2, \tag{29}$$

with boundary conditions

$$\Psi_2 = \Psi_1, \qquad D_2 \frac{\partial \Psi_2}{\partial \nu} = D_1 \frac{\partial \Psi_1}{\partial \nu} \qquad \text{on } \Gamma, \tag{30}$$

$$\Psi_1 + 2\alpha D_1 \frac{\partial \Psi_1}{\partial \nu} = 0 \quad \text{on } \partial\Omega. \tag{31}$$

Using these relations in Green's formula (27) and using (21), (22) we get

$$\left\langle \mathcal{M}\Phi_1^\delta, \zeta \right\rangle_Z = -\int_{\Omega_1} \Phi_1^\delta \overline{\mathcal{M}^*\zeta} \, d\mathbf{r} + \int_{\partial\Omega} \left(\overline{\Psi}_1 D_1 \frac{\partial \Phi_1^\delta}{\partial \nu} - \Phi_1^\delta D_1 \frac{\partial \overline{\Psi}_1}{\partial \nu} \right) dS$$

$$+ \int_{\Gamma} \left(-\overline{\Psi}_1 D_1 \frac{\partial \Phi_1^\delta}{\partial \nu} + \Phi_1^\delta D_1 \frac{\partial \overline{\Psi}_1}{\partial \nu} \right) dS$$

$$+ \int_{\Gamma} \left(\overline{\Psi}_2 D_2 \frac{\partial \Phi_2^\delta}{\partial \nu} - \Phi_2^\delta D_2 \frac{\partial \overline{\Psi}_2}{\partial \nu} \right) dS + \left\langle \Phi_1^\delta, \mathcal{M}^*\zeta \right\rangle_F. \tag{32}$$

Obviously the first and the last terms on the right-hand side cancel each other. The second term on the right-hand side disappears because of (7) and (31). Applying to the remaining

expressions on the right-hand side the conditions (23)–(25) we find that

$$
\begin{aligned}
\left\langle \mathcal{M}\Phi_1^\delta, \zeta \right\rangle_Z &= \int_\Gamma \left(-\overline{\Psi}_1 D_1 \frac{\partial \Phi_1^\delta}{\partial \nu} + \Phi_1^\delta D_1 \frac{\partial \overline{\Psi}_1}{\partial \nu} \right) \mathrm{d}S + \int_\Gamma \left(\overline{\Psi}_2 D_2 \frac{\partial \Phi_2^\delta}{\partial \nu} - \Phi_2^\delta D_2 \frac{\partial \overline{\Psi}_2}{\partial \nu} \right) \mathrm{d}S \\
&= -\int_\Gamma \left(D_1 \frac{\partial \Phi_1^\delta}{\partial \nu} - D_2 \frac{\partial \Phi_2^\delta}{\partial \nu} \right) \overline{\Psi}_1 \, \mathrm{d}S + \int_\Gamma D_1 \frac{\partial \overline{\Psi}_1}{\partial \nu} \left(\Phi_1^\delta - \Phi_2^\delta \right) \mathrm{d}S \\
&= -\int_\Gamma \left(-h_{\hat{\nu}}\left(D_1 k_1^2 - D_2 k_2^2 \right) \Phi + \nabla_\parallel \cdot [h_{\hat{\nu}}(D_1 \nabla_\parallel \Phi_1 - D_2 \nabla_\parallel \Phi_2)] \right) \overline{\Psi}_1 \, \mathrm{d}S \\
&\quad + \int_\Gamma D_1 \frac{\partial \overline{\Psi}_1}{\partial \nu} (-h_{\hat{\nu}}) \left(\frac{\partial \Phi_1}{\partial \nu} - \frac{\partial \Phi_2}{\partial \nu} \right) \mathrm{d}S.
\end{aligned}
\tag{33}
$$

Using

$$
-h_{\hat{\nu}} D_1 \left(\frac{\partial \Phi_1}{\partial \nu} - \frac{\partial \Phi_2}{\partial \nu} \right) = h_{\hat{\nu}} \frac{D_1}{D_2} (D_1 - D_2) \frac{\partial \Phi_1}{\partial \nu},
$$

applying the divergence theorem to the second term of the integral in line (33), taking into account that the spaces where our inner products are defined are complex valued and using $\mathcal{R}'(\Gamma) h_{\hat{\nu}} = \mathcal{M}\Phi_1^\delta$, we end up with

$$
\langle \mathcal{R}'(\Gamma) h_{\hat{\nu}}, \zeta \rangle_Z = \left\langle h_{\hat{\nu}}, \overline{\left(D_1 k_1^2 - D_2 k_2^2 \right)} \overline{\Phi} \Psi + (D_1 - D_2) \left[\frac{D_1}{D_2} \frac{\overline{\partial \Phi_1}}{\partial \nu} \frac{\partial \Psi_1}{\partial \nu} + \overline{\nabla_\parallel \Phi} \cdot \nabla_\parallel \Psi \right] \right\rangle_\Gamma,
\tag{34}
$$

where the notation $\langle, \rangle_\Gamma$ indicates that the considered quantities are actually restricted to the interface Γ, a well-known result from shape sensitivity analysis (see, for example, [50]). Observing that $D_1 k_1^2 - D_2 k_2^2 = \mu_{\mathrm{a},1} - \mu_{\mathrm{a},2}$ is actually real (due to (8)), and using the definition of the adjoint (26), we can identify now

$$
\begin{aligned}
\mathcal{R}'^*(\Gamma)\zeta &= (\mu_{\mathrm{a},1} - \mu_{\mathrm{a},2})\overline{\Phi}\Psi + (D_1 - D_2) \left[\frac{D_1}{D_2} \frac{\overline{\partial \Phi_1}}{\partial \nu} \frac{\partial \Psi_1}{\partial \nu} + \overline{\nabla_\parallel \Phi} \cdot \nabla_\parallel \Psi \right] \\
&= (\mu_{\mathrm{a},1} - \mu_{\mathrm{a},2})\overline{\Phi}\Psi + (D_1 - D_2)\overline{\nabla \Phi_2} \cdot \nabla \Psi_1,
\end{aligned}
\tag{35}
$$

which is understood to be evaluated at the interface Γ due to (34). (See also the discussion in [44]: the shape derivative can be interpreted as a surface measure concentrated on the interface Γ. Formally, we can extend (35) to the entire domain P by multiplication with the Dirac delta distribution concentrated on Γ. For more details see [18].) Here we dropped subindices where the corresponding quantities are continuous (which includes the tangential gradients) at Γ and we used

$$
\nabla \Phi_2 = \frac{\partial \Phi_2}{\partial \nu} \hat{\nu} + \nabla_\parallel \Phi_2,
\tag{36}
$$

$$
\nabla \Psi_1 = \frac{\partial \Psi_1}{\partial \nu} \hat{\nu} + \nabla_\parallel \Psi_1, \qquad \hat{\nu} \cdot \nabla_\parallel = 0.
\tag{37}
$$

4. Implementation

In this section we give a few more technical details on how we have implemented the forward problem and its linearization.

4.1. The forward problem: boundary integral equation

Since the boundaries Γ_ℓ are the unknowns of the inverse problem under consideration, we adopt a boundary integral equations (BIE) representation for the forward model. We introduce the following notation:

$$U_\ell := \Phi_{\ell-1}|_{\Gamma_\ell} = \Phi_\ell|_{\Gamma_\ell}, \tag{38}$$

$$V_\ell := D_{\ell-1} \left.\frac{\partial \Phi_{\ell-1}}{\partial \nu_{\ell-1}}\right|_{\Gamma_\ell} = -D_\ell \left.\frac{\partial \Phi_\ell}{\partial \nu_\ell}\right|_{\Gamma_\ell} \equiv D_{\ell-1} \left.\frac{\partial \Phi_{\ell-1}}{\partial \nu}\right|_{\Gamma_\ell} = D_\ell \left.\frac{\partial \Phi_\ell}{\partial \nu}\right|_{\Gamma_\ell}. \tag{39}$$

As in section 3 we consider the simplified case of only two regions. For a more general implementation we refer to [47]. For homogeneous region Ω_1, Ω_2, making use of the definition of the normals in section 3, Green's second theorem provides the following:

$$\Phi_1(\mathbf{r}; \omega) + \int_{\partial\Omega} \left(\frac{\partial G_1(\mathbf{r}, \mathbf{r}'; \omega)}{\partial \nu} + \frac{G_2(\mathbf{r}, \mathbf{r}'; \omega)}{2\alpha D_1} \right) U_1(\mathbf{r}'; \omega) \, dS(\mathbf{r}')$$
$$- \int_\Gamma \left(\frac{\partial G_1(\mathbf{r}, \mathbf{r}'; \omega)}{\partial \nu} U_2(\mathbf{r}'; \omega) - \frac{G_1(\mathbf{r}, \mathbf{r}'; \omega)}{D_1} V_2(\mathbf{r}'; \omega) \right) dS(\mathbf{r}') = Q_1(\mathbf{r}; \omega) \tag{40}$$

$$\Phi_2(\mathbf{r}; \omega) + \int_\Gamma \left(\frac{\partial G_2(\mathbf{r}, \mathbf{r}'; \omega)}{\partial \nu} U_2(\mathbf{r}'; \omega) - \frac{G_2(\mathbf{r}, \mathbf{r}'; \omega)}{D_2} V_2(\mathbf{r}'; \omega) \right) dS(\mathbf{r}') = Q_2(\mathbf{r}; \omega), \tag{41}$$

where

$$Q_\ell(\mathbf{r}; \omega) = \int_{\Omega_\ell} G_\ell(\mathbf{r}, \mathbf{r}'; \omega) q_\ell(\mathbf{r}') \, d^n\mathbf{r}' \tag{42}$$

and the fundamental solutions G_ℓ are the three-dimensional Green's functions of the diffusion equation in an infinite medium which take the form of spherical waves

$$G_\ell(\mathbf{r}, \mathbf{r}', \omega) = \frac{1}{4\pi|\mathbf{r} - \mathbf{r}'|} e^{-k_\ell|\mathbf{r}-\mathbf{r}'|}. \tag{43}$$

Taking the limit as $\mathbf{r} \in \Omega_1 \to \partial\Omega$, $\mathbf{r} \in \Omega_1 \to \Gamma$ and $\mathbf{r} \in \Omega_2 \to \Gamma$ results in three coupled BIEs in the three unknown functions

$$\{f\} = \{U_1, U_2, V_2\}, \tag{44}$$

whose form is given by

$$\xi_1^+(\mathbf{r})U_1(\mathbf{r}; \omega) + \int_{(\partial\Omega-\sigma_\varepsilon^+)} \left(\frac{\partial G_1(\mathbf{r}, \mathbf{r}'; \omega)}{\partial \nu} + \frac{G_1(\mathbf{r}, \mathbf{r}'; \omega)}{2\alpha D_1} \right) U_1(\mathbf{r}'; \omega) \, dS(\mathbf{r}')$$
$$- \int_\Gamma \left(\partial_1 G_1(\mathbf{r}, \mathbf{r}'; \omega) U_2(\mathbf{r}'; \omega) - \frac{G_1(\mathbf{r}, \mathbf{r}'; \omega)}{D_1} V_2(\mathbf{r}'; \omega) \right) dS(\mathbf{r}') = Q_1(\mathbf{r}; \omega) \tag{45}$$

$$\xi_1^-(\mathbf{r})U_2(\mathbf{r}; \omega) + \int_{\partial\Omega} \left(\frac{\partial G_1(\mathbf{r}, \mathbf{r}'; \omega)}{\partial \nu} + \frac{G_1(\mathbf{r}, \mathbf{r}'; \omega)}{2\alpha D_1} \right) U_1(\mathbf{r}'; \omega) \, dS(\mathbf{r}')$$
$$- \int_{(\Gamma-\sigma_\varepsilon^-)} \left(\partial_1 G_1(\mathbf{r}, \mathbf{r}'; \omega) U_2(\mathbf{r}'; \omega) - \frac{G_1(\mathbf{r}, \mathbf{r}'; \omega)}{D_1} V_2(\mathbf{r}'; \omega) \right) dS(\mathbf{r}')$$
$$= Q_1(\mathbf{r}; \omega) \tag{46}$$

$$\xi_2^+(\mathbf{r})U_2(\mathbf{r}; \omega) + \int_{(\Gamma-\sigma_\varepsilon^+)} \left(\frac{\partial G_2(\mathbf{r}, \mathbf{r}'; \omega)}{\partial \nu} U_2(\mathbf{r}'; \omega) - \frac{G_2(\mathbf{r}, \mathbf{r}'; \omega)}{D_2} V_2(\mathbf{r}'; \omega) \right) dS(\mathbf{r}') = 0, \tag{47}$$

where we assumed that the source term is only in Ω_1. The extra function $\xi_\ell^\pm(\mathbf{r})$ in (45)–(47) arises due to singularities on the boundary. These terms can be calculated by surrounding the point $\mathbf{r}$, which lies on the boundary, by a small hemisphere σ_ε of radius ε and taking the limit when $\varepsilon \to 0$. However, as shown in [6, 9], this term can be obtained indirectly by utilizing some simple physical considerations. In particular, we have $\xi_i^+(\mathbf{r}) = \xi_i^-(\mathbf{r}) = \frac{1}{2}$ when the observation point lies on a smooth surface, which is the case considered here.

4.2. Discretization by a boundary element method

The interfaces Γ_ℓ are discretized to meshes

$$\mathbb{V}_\ell = \{\mathbb{T}_\ell, \mathbb{N}_\ell, \mathbb{U}_\ell\}$$

where $\mathbb{T}_\ell$ is the set of P_ℓ surface elements $\tau_{\ell,e}$; $e = 1, \ldots, P_\ell$, $\mathbb{N}_\ell$ is the set of N_ℓ vertices $\mathbf{N}_{\ell,p}$; $p = 1, \ldots, N_\ell$ and $\mathbb{U}_\ell$ is the set of N_ℓ locally supported basis functions $\psi_{\ell,p}(\mathbf{r})$; $p = 1, \ldots, N_\ell$. Then functions (38), (39) are represented as

$$U_\ell(\mathbf{r}; \omega) \approx \sum_{p=1}^{N_\ell} U_{\ell,p}(\omega)\psi_{\ell,p}(\mathbf{r}), \qquad V_\ell(\mathbf{r}; \omega) \approx \sum_{p=1}^{N_\ell} V_{\ell,p}(\omega)\psi_{\ell,p}(\mathbf{r}). \quad (48)$$

Using the representation (48) in the BIE system (45)–(47) followed by sampling at the nodal points, we obtain a discrete system known as collocation boundary element method [2, 6, 7, 48, 49] to construct a linear matrix equation

$$\begin{pmatrix} \frac{1}{2}\mathsf{I} + \mathsf{A}_{11}^{(1)} + \frac{1}{2\alpha}\mathsf{B}_{11}^{(1)} & -\mathsf{A}_{12}^{(1)} & \mathsf{B}_{12}^{(1)} \\ \mathsf{A}_{11}^{(2)} + \frac{1}{2\alpha}\mathsf{B}_{11}^{(2)} & \frac{1}{2}\mathsf{I} - \mathsf{A}_{12}^{(2)} & \mathsf{B}_{12}^{(2)} \\ 0 & \frac{1}{2}\mathsf{I} + \mathsf{A}_{22}^{(2)} & -\mathsf{B}_{22}^{(2)} \end{pmatrix} \begin{pmatrix} \mathbf{U}_1 \\ \mathbf{U}_2 \\ \mathbf{V}_2 \end{pmatrix} = \begin{pmatrix} \mathbf{Q}_1|_{\partial\Omega} \\ \mathbf{Q}_1|_\Gamma \\ 0 \end{pmatrix} \quad (49)$$

with $\mathbf{U}_\ell, \mathbf{V}_\ell$ being the vectors of coefficients $U_{\ell,p}(\omega)$, $V_{\ell,p}(\omega)$ in (48), and matrix elements given by

$$A_{11}^{(j)}(p, p') = \int_{\partial\Omega} \frac{\partial G_1(\mathbf{N}_{j,p}, \mathbf{r}'; \omega)}{\partial\nu}\psi_{1,p'}(\mathbf{r}')\,\mathrm{d}S(\mathbf{r}')$$

$$A_{12}^{(j)}(p, p') = \int_\Gamma \frac{\partial G_1(\mathbf{N}_{j,p}, \mathbf{r}'; \omega)}{\partial\nu}\psi_{2,p'}(\mathbf{r}')\,\mathrm{d}S(\mathbf{r}')$$

$$A_{22}^{(j)}(p, p') = \int_\Gamma \frac{\partial G_2(\mathbf{N}_{j,p}, \mathbf{r}'; \omega)}{\partial\nu}\psi_{2,p'}(\mathbf{r}')\,\mathrm{d}S(\mathbf{r}')$$

$$B_{11}^{(j)}(p, p') = \int_{\partial\Omega} \frac{G_1(\mathbf{N}_{j,p}, \mathbf{r}'; \omega)}{D_1}\psi_{1,p'}(\mathbf{r}')\,\mathrm{d}S(\mathbf{r}')$$

$$B_{12}^{(j)}(p, p') = \int_\Gamma \frac{G_1(\mathbf{N}_{j,p}, \mathbf{r}'; \omega)}{D_1}\psi_{2,p'}(\mathbf{r}')\,\mathrm{d}S(\mathbf{r}')$$

$$B_{22}^{(j)}(p, p') = \int_\Gamma \frac{G_2(\mathbf{N}_{j,p}, \mathbf{r}'; \omega)}{D_2}\psi_{2,p'}(\mathbf{r}')\,\mathrm{d}S(\mathbf{r}').$$

Note that appropriate numerical techniques for handling the singularity of the kernels are required for the diagonal elements of these matrices [47]. We represent (49) as

$$\mathsf{T}\mathbf{f} = \mathbf{Q}, \quad (50)$$

where $\mathbf{f} = [\mathbf{U}_1, \mathbf{U}_2, \mathbf{V}_2]$ is the discrete version of $\{\mathbf{f}\}$ in (44). The matrix T takes the form of a dense un-symmetric block matrix. The corresponding system is solved using a preconditioned GMRES solver. For each source position q_j we construct the right-hand side vector $\mathbf{Q}^{(j)}$ and solve the linear system (50) and use the measurement operator $\mathcal{M} : \mathbb{C}^{N_1} \to \mathbb{C}^M$ from (13) to get the measurements $\mathbf{g}^{(j)}$.

4.3. Construction of the Jacobian

The component $J_{ij,k}$ of the Jacobian represents the variation of the ith measurement of the jth source with respect to the kth shape basis function. We take $q^{(j)}$ to be the source distributions and ζ to be the sampling functions w_i from (14), whence the BIE formulation to the forward problem yields a set of functions (cf (44))

$$\{f^{(j)}\} = \left\{ U_1^{(j)}, U_2^{(j)}, V_2^{(j)} \right\}$$

and to the adjoint problem yields a set

$$\{f^{+(i)}\} = \left\{ U_1^{+(i)}, U_2^{+(i)}, V_2^{+(i)} \right\},$$

where we introduced the notation (cf (38), (39))

$$U_2^+ := \Psi_2|_\Gamma = \Psi_1|_\Gamma, \tag{51}$$

$$V_2^+ := D_2 \frac{\partial \Psi_2}{\partial \nu}\bigg|_\Gamma = D_1 \frac{\partial \Psi_1}{\partial \nu}\bigg|_\Gamma. \tag{52}$$

Making use of (34) we write

$$J_{ij,k} = -\langle \mathcal{R}'_j[\gamma_k], w_i \rangle_Z = \left\langle \gamma_k, -(\mu_{a,1} - \mu_{a,2}) \overline{U}^{(j)} U^{+(i)} \right.$$
$$\left. - (D_1 - D_2) \left[\frac{1}{D_1 D_2} \overline{V}_2^{(j)} V_2^{+(i)} + \nabla_\| \overline{U}_2^{(j)} \cdot \nabla_\| U_2^{+(i)} \right] \right\rangle_\Gamma. \tag{53}$$

Using the same representation (48) for the adjoint functions we get

$$J_{ij,k} = -(\mu_{a,1} - \mu_{a,2}) \sum_{p,p'} \overline{U}_{2,p}^{(j)} U_{2,p'}^{+(i)} \int_\Gamma \gamma_k \psi_{2,p} \psi_{2,p'} \, dS$$
$$- (D_1 - D_2) \frac{1}{D_2 D_1} \sum_{p,p'} \overline{V}_{2,p}^{(j)} V_{2,p'}^{+(i)} \int_\Gamma \gamma_k \psi_{2,p} \psi_{2,p'} \, dS$$
$$- (D_1 - D_2) \overline{U}_{2,p}^{(j)} U_{2,p'}^{+(i)} \int_\Gamma \gamma_k \nabla_\| \psi_{2,p} \cdot \nabla_\| \psi_{2,p'} \, dS \tag{54}$$

and introducing a similar vector notation as in (49) we get

$$J_{ij,k} = -(\mu_{a,1} - \mu_{a,2}) \overline{\mathbf{U}}_2^{+(i)} \cdot \mathsf{E}^{(k)} \mathbf{U}_2^{(j)} - (D_1 - D_2) \frac{1}{D_2 D_1} \overline{\mathbf{V}}_2^{+(i)} \cdot \mathsf{E}^{(k)} \mathbf{V}_2^{(i)}$$
$$- (D_1 - D_2) \overline{\mathbf{U}}_2^{+(i)} \cdot \mathsf{F}^{(k)} \mathbf{U}_2^{(j)}. \tag{55}$$

The matrices $\mathsf{E}^{(k)}$ and $\mathsf{F}^{(k)}$ are sparse having non-zero elements only where the basis functions $\psi_{2,p}$ and $\psi_{2,p'}$ have overlapping support. They are given by

$$E_{pp'}^{(k)} = \int_\Gamma \gamma_k \psi_{2,p} \psi_{2,p'} \, dS, \tag{56}$$

$$F_{pp'}^{(k)} = \int_\Gamma \gamma_k \nabla_\| \psi_{2,p} \cdot \nabla_\| \psi_{2,p'} \, dS. \tag{57}$$

They can be constructed element wise using the same machinery for the construction of the BEM matrices, and are constant at each iteration of the inverse problem, before Γ is updated and re-meshed.

We note here that we can write an equivalent expression

$$J_{ij,k} = -\bar{\mathbf{f}}^{+(i)} \cdot \begin{pmatrix} 0 & 0 & 0 \\ 0 & \delta\mu_a\mathsf{E}^{(k)} + \delta D\mathsf{F}^{(k)} & 0 \\ 0 & 0 & \frac{\delta D}{D_1 D_2}\mathsf{F}^{(k)} \end{pmatrix} \mathbf{f}^{(j)}$$

$$= -(\mathsf{T}^{-1}\mathbf{w}^{(i)}) \cdot \frac{\partial\mathsf{T}}{\partial\gamma_k}\mathsf{T}^{-1}\mathbf{Q}^{(j)}, \tag{58}$$

where the component $\delta\mu_a\mathsf{E}^{(k)} + \delta D\mathsf{F}^{(k)}$ of the discrete derivative $\frac{\partial\mathsf{T}}{\partial\gamma_k}$ is identical to expressions (31), (32) of [30]. The extra term $\frac{\delta D}{D_1 D_2}\mathsf{F}^{(k)}$ arises because of the discontinuity in the normal derivatives which is explicitly represented in the BEM framework.

4.4. Data rescaling

In practice the measurements in the frequency domain experiment for DOT are complex numbers, that is $\mathbf{g} \in \mathbb{C}^{MS}$, where M is the total number of detectors and S is the total number of the sources. We use the following representation for $\mathbf{g}$:

$$\mathbf{g} = \mathrm{Re}[\mathbf{g}] + \mathrm{i}\,\mathrm{Im}[\mathbf{g}] = \|\mathbf{g}\|\exp\{\mathrm{i}\,\mathrm{arg}(\mathbf{g})\}, \tag{59}$$

where

$$\|\mathbf{g}\| = (\mathrm{Re}[\mathbf{g}]^2 + \mathrm{Im}[\mathbf{g}]^2)^{\frac{1}{2}} \tag{60}$$

is the *amplitude* of the data, and

$$\mathrm{arg}(\mathbf{g}) = \arctan\left(\frac{\mathrm{Im}[\mathbf{g}]}{\mathrm{Re}[\mathbf{g}]}\right) \tag{61}$$

is the *phase*. Then, by taking the log of (59), we get

$$\log(\mathbf{g}) = \log(\|\mathbf{g}\|) + \mathrm{i}\,\mathrm{arg}(\mathbf{g}). \tag{62}$$

Finally, we assemble the data as

$$\tilde{\mathbf{g}} = \begin{pmatrix} \log(\|\mathbf{g}\|) \\ \mathrm{arg}(\mathbf{g}) \end{pmatrix}. \tag{63}$$

This logarithmic scaling reduces the difference in the magnitude of the values for amplitude and phase data. Taking the residual in the scaled data results in

$$\tilde{\Xi}(\gamma) = \|\log(\mathbf{g}) - \log(\mathcal{K}(\gamma))\|^2. \tag{64}$$

The scaled and split Jacobian $\tilde{\mathsf{J}}$ will then be

$$\tilde{\mathsf{J}}(\gamma) = \begin{pmatrix} \mathrm{Re}\big[\mathrm{diag}\big(\frac{1}{\mathcal{K}(\gamma)}\big)\mathsf{J}(\gamma)\big] \\ \mathrm{Im}\big[\mathrm{diag}\big(\frac{1}{\mathcal{K}(\gamma)}\big)\mathsf{J}(\gamma)\big] \end{pmatrix}. \tag{65}$$

5. Numerical results from 3D simulations

We consider numerical results of the proposed method for three-dimensional reconstructions in diffusive optical tomography with frequency domain data. In the following subsections we will discuss the capabilities and the weaknesses of the proposed method with an emphasis on medical applications. In particular, we will begin the reconstruction of a small inclusion for a realistic head geometry. Then, the reconstruction of a large, non-convex inclusion will be attempted in order to address the problem of the extraction of structural information for tissue from optical measurements on the surface. Finally, an attempt is made to test the simultaneous recovery of both optical and shape coefficients.
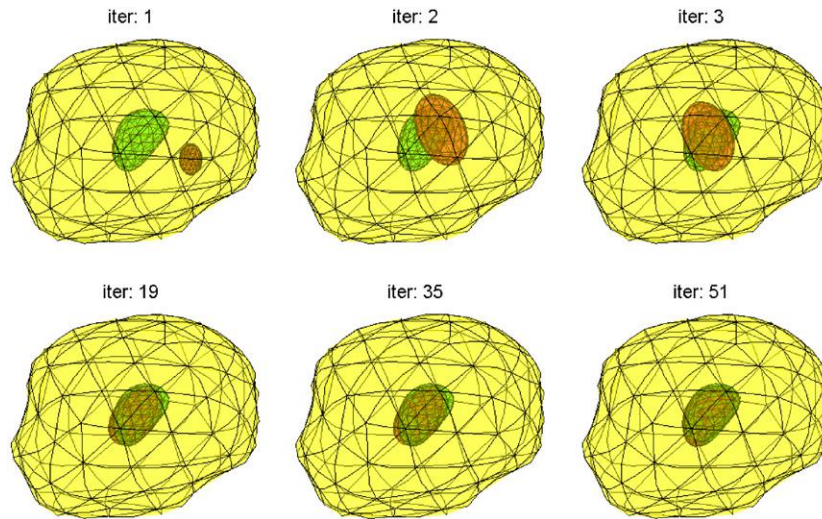
Figure 5. Example 1: recovery of inhomogeneity shape from OT measurements on the surface with known *a priori* optical parameters. The target is the green shape described with 48 spherical harmonic parameters, and the reconstructed shape is red. The reconstruction starts with 12 spherical harmonics and continues by increasing it up to 48.

M An AVI movie of this figure is available from stacks.iop.org/IP/22/1509

5.1. Example 1: region recovery inside homogeneous medium

In this experimental setup, a geometric model for an infant's head is created and treated as a homogeneous domain. We use a mesh of 362 nodes and 180 surface elements to model the external surface of the head. The optical parameters chosen for the homogeneous background are set to $\mu_a = 0.01$ mm^{-1} and $\mu'_s = 1$ mm^{-1}.

In the interior of the head an arbitrary-shaped inhomogeneity Ω_2 with optical properties of $\mu_a = 0.02$ mm^{-1} and $\mu'_s = 2$ mm^{-1} is embedded. Its surface is described by 16 spherical harmonic coefficients $\gamma^\diamond$ for each Cartesian coordinate x, y, z. This defines a parametric surface using up to third degree spherical harmonics. A regular mesh with 180 elements and 362 nodes is mapped onto that surface to create the discrete approximation necessary for the BEM calculation, see figure 5.

Using this geometric setup, we assign 20 sources and 20 detector positions on the surface of the head as shown in figure 2. The modulation frequency of the sources is set to 100 MHz. Synthetic data are then collected at the 20 detectors using the forward model $\mathcal{K}(\gamma^\diamond, \mu_a^\diamond, D^\diamond)$ with one source illuminated at a time. Gaussian random noise with a standard deviation of 1% of the measured signal is added to these data.

As the initial guess for the inverse problem we select a closed surface centred at a random position. In this case, we start with four parameters for each direction in a first degree spherical harmonic description. This choice leads to a search space of dimension $3 \times 4 = 12$. The optimization continues until a local minimum has been reached and then an extra degree of spherical harmonics is added to the description. The addition of degrees is continued until the final shape is constructed with third degrees of spherical harmonics which matches the degrees used for the simulated data object.

In figure 5 we can observe the reconstruction procedure. The initial iterations worked towards the recovery of the centre of the object and the shape, while further iterations and the addition of the higher degrees of spherical harmonics drive the recovery of finer details.
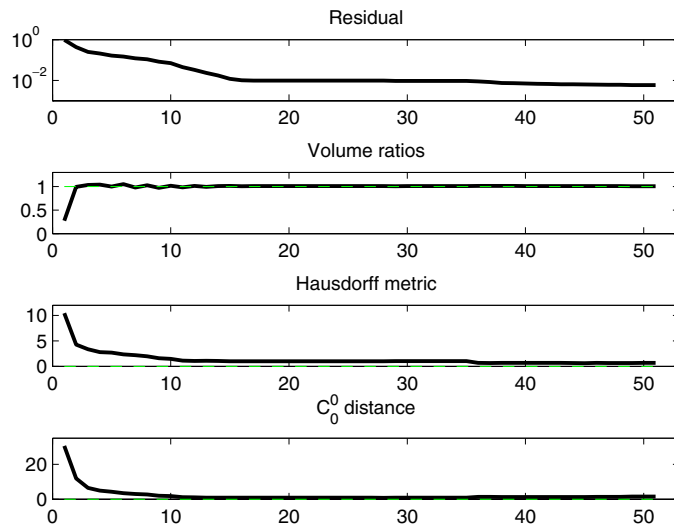
Figure 6. Example 1: evolution of different measures with iteration. Shown from top to bottom are the data residual of the optimization, the volume ratios between target and reconstructed shape, the Hausdorff measure for the mismatch between the surfaces of the shapes and the distance between the centre of the target object and the reconstructed one.

To assess the success of the recovery of the inhomogeneity we measure the residual of the data $\|\log(\mathbf{g}) - \log(\mathcal{K}(\gamma, \mu_a, D))\|^2$ which can be seen in the top row of figure 6 plotted in a log scale. The residual is decreased during the first iterations until a local minimum is reached and then the addition of further degrees of spherical harmonics allows it to reduce further.

The volume of the object recovered is the second measure that we used. To calculate the volume the object is divided into tetrahedra based on the mapped mesh and the volume of all the tetrahedra is added to calculate the total volume of the object. The initial volume of the target object is 109.8159 mm^3 while the volume of the starting shape for the reconstructed object is 30.0728 mm^3. The second row of the figure shows the ratio of the volume of the reconstruction shape in each iteration to the volume of the target shape. The final reconstructed shape has a volume of 110.5494 mm^3 giving a good approximation of the target volume.

The next row of figure 6 shows the Hausdorff distance $H(\Gamma^\diamond, \Gamma^{(n)})$ between the target surface $\Gamma^\diamond$ and the estimated surface $\Gamma^{(n)}$ in iteration n. The Hausdorff distance measures the degree of mismatch between the two sets $\mathbb{N}^\diamond, \mathbb{N}^{(n)}$, as the distance of the point of $\mathbb{N}^\diamond$ that is farthest from any point of $\mathbb{N}^{(n)}$ and is defined as

$$H(\Gamma^\diamond, \Gamma^{(n)}) = \max_{\mathbf{N} \in \Gamma^\diamond} \min_{\mathbf{N}' \in \Gamma^{(n)}} |\mathbf{N} - \mathbf{N}'|.$$

Finally, the zeroth degree of the spherical harmonic representation, which represents the centre of the objects, is used in the fourth row of figure 6. The plot is of the distance between the centre of the target and reconstructed object.

$$C_0^0(\Gamma^\diamond, \Gamma^{(n)}) = |\mathbf{c}^\diamond - \mathbf{c}^{(n)}|$$

with $\mathbf{c}$ given by (10).

As can be seen, the location and the approximate shape of the simple 3D inclusion can be recovered with good accuracy from noisy data. The centre and the size of the object is reconstructed within the first iterations as the C_0^0 and Hausdorff distance indicate, and the optimization continues with the finer details.
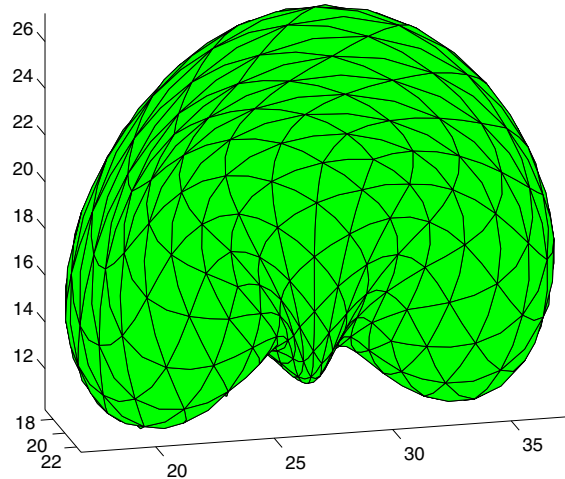
Figure 7. Example 2: target shape.

5.2. Example 2: recovery of large non-convex object

As a second example we consider the larger object shown in figure 7. The volume of this object is 1082.5 mm^3 making it more than ten times bigger than that in the example of section 5.1. In this case a non-convex object was chosen to show the capabilities of the spherical harmonic representation. The complexity of the object was described by 48 spherical harmonic parameters for the third degree description. For the mapping we used a larger mesh of 500 elements and 1002 nodes. Position of sources and detectors, modulation frequency and added noise in the data was as in the example of section 5.1.

In figures 8 and 9 we show the evolution of the shape and the corresponding metrics as in figures 5 and 6. To show more clearly the higher order shape recovery we show in figure 10 the approximations of the reconstructed shape to first, second and third degrees.

5.3. Example 3: recovery of optical coefficients and shape parameters

This experiment extends the shape recovery method to the situation where the values of μ_a and μ_s' are also considered as unknown variables. More precisely, the simulated data are created assuming the optical properties $\mu_a^\diamond = 0.02$ mm^{-1} and $\mu_s'^\diamond = 2$ mm^{-1} for the region Ω_2, and $\mu_a^\diamond = 0.01$ mm^{-1} and $\mu_s'^\diamond = 1$ mm^{-1} for the homogeneous background. The geometric setup is as given in section 5.1. There was no added noise in this example.

In this case we allow the reconstruction to use only first degree spherical harmonics leading to a search space of 12 parameters for the shape and 2 parameters for the optical properties. The strategy that we decided to use combines four iterations of shape optimization alone and then one of optimizing the optical parameters on their own. This alternation strategy prevents the optical properties to move far from the desired value while the shape is still far from the correct one.

For the derivatives $\frac{\partial \mathcal{K}(\gamma, \mu_a, D)}{\partial \mu_a}$ and $\frac{\partial \mathcal{K}(\gamma, \mu_a, D)}{\partial \mu_s}$ of the forward operator with respect to the absorption and scattering coefficients for the subregion Ω_2 we use a straightforward finite differencing scheme, running two additional forward problems on slightly perturbed optical parameter values inside this subregion.

We chose the initial optical parameters as seen in the first two columns of table 1 so that they represent all possible situations for underestimation or overestimation of one or both of
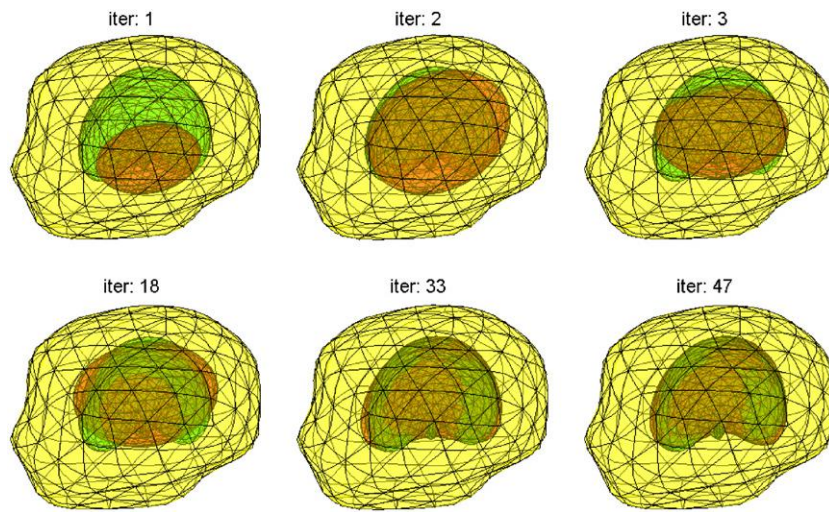
Figure 8. Example 2: recovery of shape of a large non-convex object. The reconstruction scheme is as in figure 5.

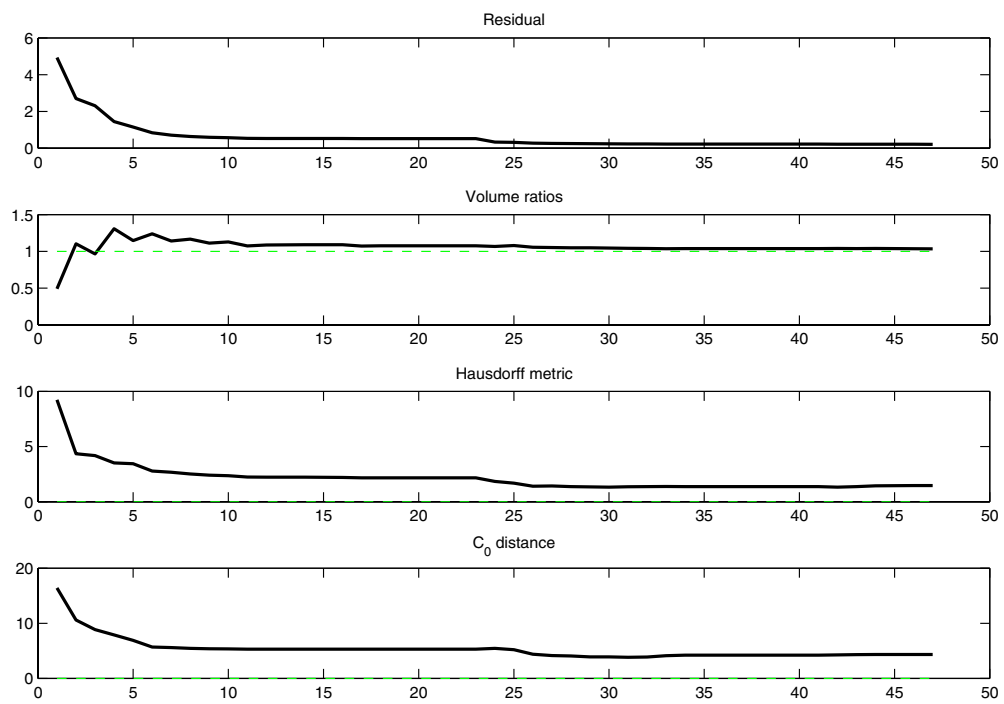M An AVI movie of this figure is available from stacks.iop.org/IP/22/1509

Figure 9. Example 2: evolution of the reconstruction metrics for the large non-convex object. The measures are the same as figure 6.

the μ_a, μ_s'. The next two columns of the table show the reconstructed values after the evolution of the shape and then the centres' distances, the Hausdorff distance, and the volume ratios at the last iteration of the evolution.
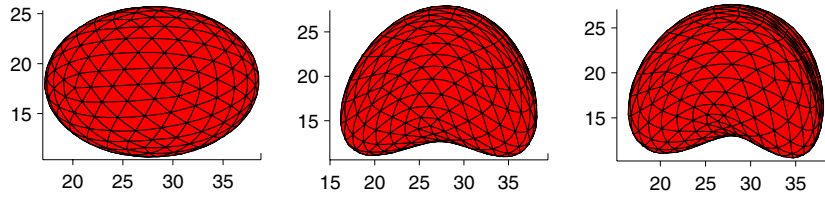
Figure 10. Example 2: the reconstructed shape using up to first, second and third degrees of spherical harmonics.

Table 1. Example 3: some experiments with simultaneous reconstruction for shape and optical parameters.

$\mu_a^{(0)}$	$\mu_s'^{(0)}$	$\hat{\mu}_a$	$\hat{\mu}_s$	$C_0^0(\Gamma^\diamond, \hat{\Gamma})$	$H(\Gamma^\diamond, \hat{\Gamma})$	Vol.	C_{μ_a}	C_D
0.015	2	0.017 138	1.6738	0.995 64	0.945 78	1.3403	0.956 68	0.903 59
0.017	1.7	0.018 049	1.7492	0.959 31	0.918 63	1.2204	0.982 31	0.914 97
0.017	2.2	0.018 037	1.7602	0.937 94	0.872 08	1.2138	0.975 57	0.923 25
0.02	2.5	0.019 817	1.9459	0.829 36	0.850 07	1.032	1.0131	0.976 51
0.022	1.7	0.020 002	1.963	0.848 96	0.898 94	1.0156	1.0158	0.978 36
0.022	2.2	0.020 628	2.017	0.842 45	0.946 01	0.971 19	1.0322	0.988 12
0.025	2	0.022 298	2.1742	0.811 04	1.0684	0.868 07	1.0675	1.0197
0.025	2.5	0.023 267	2.2886	0.767 08	1.1753	0.815 21	1.0816	1.0508

The last two columns of table 1 represent measures of the product of volume and contrast as used for example in [5, 13]. We define

$$C_{\mu_a} = \frac{\hat{\mathrm{Vol}}(\Omega_2)(\mu_{a,1} - \hat{\mu}_{a,2})}{\mathrm{Vol}^\diamond(\Omega_2)(\mu_{a,1} - \mu_{a,2}^\diamond)} \tag{66}$$

$$C_D = \frac{\hat{\mathrm{Vol}}(\Omega_2)\frac{D_1}{\hat{D}_2}(D_1 - \hat{D}_2)}{\mathrm{Vol}^\diamond(\Omega_2)\frac{D_1}{D_2^\diamond}(D_1 - D_2^\diamond)}. \tag{67}$$

As can be seen, in table 1 the optical parameters and the object volumes are not recovered with complete accuracy. However, the contrast volume products given by (66) and (67) are almost constant regardless of the initial starting values. This is consistent with the predictions for diffusion coefficient contrast of [13] and for absorption coefficient contrast of [5]. However, to the best of our knowledge there are no formal results for the simultaneous reconstructions demonstrated here. Figure 11 shows the reconstructed shape (in red) for a variety of different initial guesses for the optical properties μ_a and μ_s', together with the target shape (green). We note the small variation of the shape due to the different optical properties. For illustration purposes the measurements of the evolution for the case of $\mu_a = 0.022$ and $\mu_s' = 1.7$ are presented in figure 12.

6. Conclusions and future work

In the paper we proposed a novel reconstruction scheme for a shape-based three-dimensional inverse problem for optical tomography. In our method the search space for the solution of the inverse problem is defined in terms of a spherical harmonic expansion of the unknown
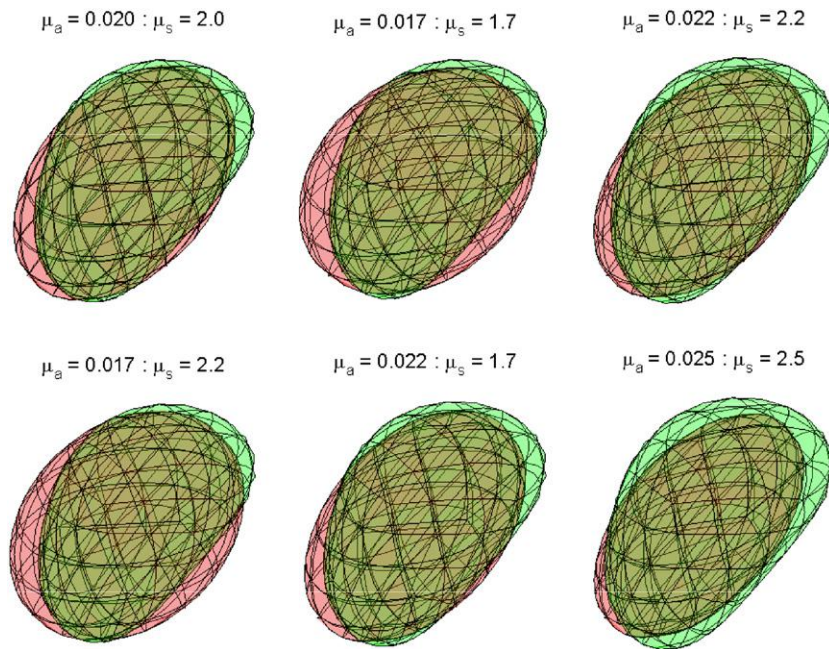
Figure 11. Example 3: the reconstructed shape (red) and the target (in green) for different cases of simultaneous recovery of shape and optical parameters.
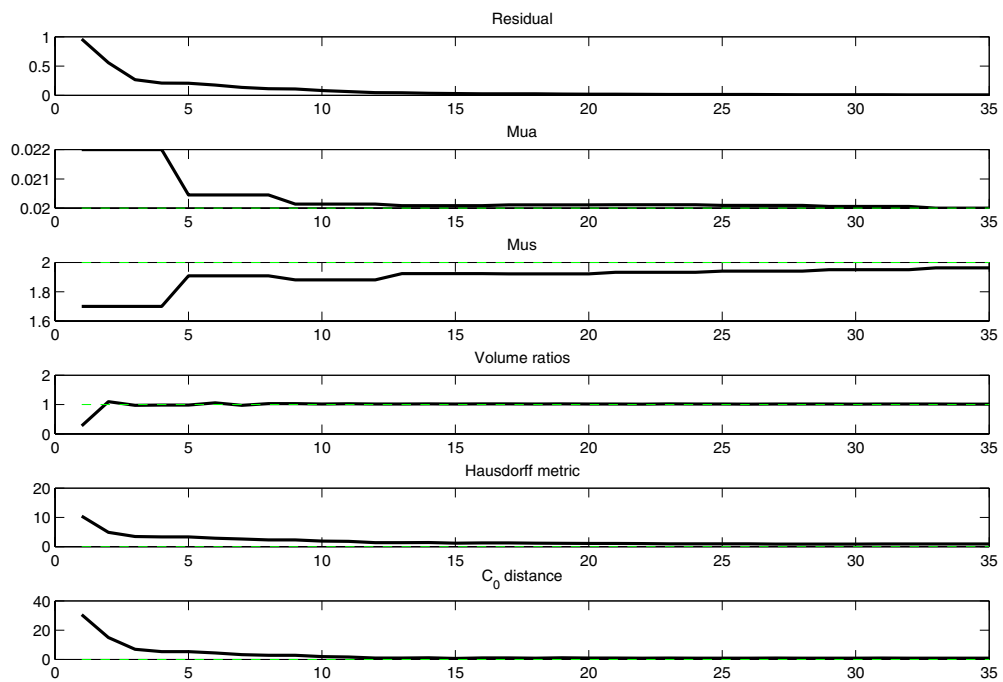

Figure 12. Example 3: the measures for the convergence of the algorithm for the example with initial $\mu_a = 0.022$ and $\mu'_s = 1.7$.

region surfaces. In doing so we incorporate in our scheme an implicit regularization where the regularization parameter is the degree of spherical harmonics used for representing the surfaces. An adjoint formulation of the parameter or shape sensitivities has been derived. In our numerical experiments we have demonstrated that our scheme is able to reconstruct in a stable and efficient way low-parametric approximations of quite complicated shapes from few given data, both for relatively small, and for relatively large regions. The simultaneous reconstruction of shape and optical parameters however is more difficult to achieve, and requires longer iteration of the reconstruction. In those situations, the shape is usually recovered well, but the final values of the reconstructed optical are not completely accurate. These findings are consistent with the predictions of asymptotic approaches which suggest that the product of recovered volume and a parameter dependent contrast function is the best that can be achieved.

Possible directions for future research are the comparison of the presented scheme with alternative shape-based techniques which use geometric penalization terms (as, for example, surface measure) instead for regularizing the inversion. More complex examples such as the reconstruction of multiple nested surfaces are also of interest, as is the application to measured, rather than simulated data.

Acknowledgments

References

[1] Aithal R and Saigal S 1995 Shape sensitivity analysis in thermal problems using BEM *Eng. Anal. Bound. Elem.* **15** 115–20
[2] Aliabadi M H 2002 *The Boundary Element Method* (New York: Wiley)
[3] Ammari H, Iakovleva E and Lesselier D 2005 A MUSIC algorithm for locating small inclusions buried in a half space from the scattering amplitude at a fixed frequency *Multiscale Mod. Sim.* **3** 597–628
[4] Arridge S R 1999 Optical tomography in medical imaging *Inverse Problems* **15** 41–93
[5] Bal G 2003 Optical tomography for small volume absorbing inclusions *Inverse Problems* **19** 371–86
[6] Becker A A 1992 *The Boundary Element Method in Engineering—A Complete Course* (New York: McGraw-Hill)
[7] Beer G 2001 *Programming the Boundary Element Method: An Introduction for Engineers* (New York: Wiley)
[8] Björck A 1996 *Numerical Methods for Least Square Problems* (Philadelphia, PA: SIAM)
[9] Bonnet M 1995 *Boundary Integral Equation Methods for Solids and Fluids* (New York: Wiley)
[10] Bonnet M 1995 Bie and material differentiation applied to the formulation of obstacle inverse problems *Eng. Anal. Bound. Elem.* **15** 121–36
[11] Brechbühler C, Gerig G and Kübler O 1995 Parametrization of closed surfaces for 3-D shape description *Comput. Vis. Image Underst.* **61** 154–70
[12] Burger M 2001 A level set method for inverse problems *Inverse Problems* **17** 1327–55

[13] Cedio-Fengya D J, Moskow S and Vogelius M S 1998 Identification of conductivity imperfections of small diameter by boundary measurements. Continuous dependence and computational reconstruction *Inverse Problems* **14** 553–95

[14] Chan T F and Tai X-C 2003 Level set and total variation regularization for elliptic inverse problems with discontinuous coefficients *J. Comput. Phys.* **193** 40–66

[15] Dorn O, Miller E and Rappaport C 2000 A shape reconstruction method for electromagnetic tomography using adjoint fields and level sets *Inverse Problems* **16** 1119–56

[16] Dorn O 2004 Shape reconstruction in scattering media with voids using a transport model and level sets *Can. Appl. Math. Q.* **10** 239–75

[17] Dorn O 2004 Shape reconstruction for an inverse radiative transfer problem arising in medical imaging *Springer Series Computational Science and Engineering (vol Numerical Methods for Multidimensional Radiative Transfer Problems)* ed R Rannacher (Berlin: Springer) at press

[18] Dorn O and Lesselier 2006 Level set methods for inverse scattering *Inverse Problems* **22** R67–R131

[19] Duraiswami R, Chanine G L and Sarkar K 1997 Boundary element techniques for efficient 2-D and 3-D electrical impedance tomography *Chem. Eng. Sci.* **52** 2185–96

[20] Duraiswami R, Sarkar K and Chanine G L 1998 Efficient 2D and 3D electrical impedance tomography using dual reciprocity boundary element techniques *Eng. Anal. Bound. Elem.* **22** 13–31

[21] Feijóo G R, Oberai A A and Pinsky P M 2004 An application of shape optimization in the solution of inverse acoustic scattering problems *Inverse Problems* **20** 199–228

[22] Ferrayé R, Dauvignac J Y and Pichot C 2003 An inverse scattering method based on contour deformations by means of a level set method using frequency hopping technique *IEEE Trans. Antennas Propag.* **51** 1100–13

[23] Gibson A P, Hebden J C and Arridge S R 2005 Recent advances in diffuse optical imaging *Phys. Med. Biol.* **50** R1–R43

[24] Guzina B B and Bonnet M 2006 Small-inclusion asymptotic for inverse problems in acoustic *Preprint*

[25] Hettlich F 1995 Frechet derivatives in inverse obstacle scattering *Inverse Problems* **11** 371–82

[26] Hettlich F and Rundell W 1996 Iterative methods for the reconstruction of the inverse potential problem *Inverse Problems* **12** 251–66

[27] Huttenlocher D P, Klanderman G A and Rucklidge W J 1993 Comparing images using the Hausdorff distance *IEEE-PAMI* **15** 850–63

[28] Ito K, Kunisch K and Li Z 2001 Level-set approach to an inverse interface problem *Inverse Problems* **17** 1225–42

[29] Kilmer M E, Miller E L, Barbaro A and Boas D 2003 3D shape-based imaging for diffuse optical tomography *Appl. Opt.* **42** 3129–44

[30] Kolehmainen V, Arridge S R, Lionheart W R B, Vauhkonen M and Kaipio J P 1999 Recovery of region boundaries of piecewise constant coefficients of an elliptic PDE from boundary data *Inverse Problems* **15** 1375–91

[31] Kolehmainen V, Arridge S R, Vauhkonen M and Kaipio J P 2000 Recovery of constant coefficients in optical diffusion tomography *Opt. Express* **7** 468–80

[32] Koo B U 1997 Shape design sensitivity analysis of acoustic problems using a boundary element method *Comput. Struct.* **65** 713–9

[33] Kortschak B and Brandstätter B 2005 A FEM-BEM approach using level-sets in electrical capacitance tomography *COMPEL* **24** 591–605

[34] Litman A, Lesselier D and Santosa D 1998 Reconstruction of a two-dimensional binary obstacle by controlled evolution of a level-set *Inverse Problems* **14** 685–706

[35] Marquardt D W 1963 An algorithm for least-squares estimation of nonlinear parameters *J. Soc. Ind. Math.* **11** 431–41

[36] Meric R A 1995 Differential and integral sensitivity formulations and shape optimisation by BEM *Eng. Anal. Bound. Elem.* **15** 181–8

[37] Natterer F and Wübbeling F 2001 Mathematical methods in image reconstruction *SIAM Monographs on Mathematical Modeling and Computation*

[38] Park S J and Kwon T H 1996 Sensitivity analysis formulation for three-dimensional conduction heat transfer with complex geometries using a boundary element method *Int. J. Numer. Methods Eng.* **39** 2837–62

[39] Potthast R 2006 A survey on sampling and probe methods for inverse problems *Inverse Problems* **22** R1–R47

[40] Press W H, Flannery B P, Teukolsky S A and Vetterling W T 2001 *Numerical Recipes in C: The Art of Scientific Computing* (Cambridge: Cambridge University Press)

[41] Ramananjaona C, Lambert M, Lesselier D and Zolésio J-P 2001 Shape reconstruction of buried obstacles by controlled evolution of a level set: from a min-max formulation to numerical experimentation *Inverse Problems* **17** 1087–111

[42] Rondi L and Santosa F 2001 Enhanced electrical impedance tomography via the Mumford–Shah functional 2001 *ESAIM: Control, Optim. Calculus Variations* **6** 517–38

[43] Van den Doel K and Ascher U M 2006 On level set regularization for highly ill-posed distributed parameter estimation problems *J. Comput. Phys.* **216** 707–23

[44] Santosa F 1996 A level-set approach for inverse problems involving obstacles *ESAIM: Control, Optim. Calculus Variations* **1** 17–33

[45] Schweiger M, Arridge S R, Hiraoka M and Delpy D T 1995 The finite element model for the propagation of light in scattering media: boundary and source conditions *Med. Phys.* **22** 1779–92

[46] Schweiger M, Arridge S R, Dorn O, Zacharopoulos A and Kolehmainen V 2006 Reconstructing absorption and diffusion shape profiles in optical tomography using a level set technique *Opt. Lett.* **31** 471–3

[47] Sikora J, Zacharopoulos A, Douiri A, Schweiger M, Horesh L, Arridge S R and Ripoll J 2006 Diffuse photon propagation in multilayered geometries *Phys. Med. Biol.* **51** 497–516

[48] Sikora J and Arridge S R 2002 Some numerical aspects of 3D BEM application to optical tomography *Proc. IV Int. Workshop Computational Problems of Electrical Engineering* pp 59–62

[49] Sikora J, Arridge S R, Ripoll J, Zacharopoulos A D and Riley J D 2004 Light propagation in diffusive media with non-scattering regions using 3D BEM *Boundary Integral Methods: Theory and Applications (University of Reading 14–18 September)*

[50] Sokolowski J and Zolésio J P 1992 *Introduction to Shape Optimization: Shape Sensitivity Analysis (Springer Series in Computational Mathematics* vol 16*)* (Berlin: Springer)

[51] Soleimani M, Lionheart W R B and Dorn O 2005 Level set reconstruction of conductivity and permittivity from boundary electrical measurements using experimental data *Inverse Problems Sci. Eng.* **14** 193–210

[52] Tortel H 2002 Localization and derivation of an optimal sphere for 3D perfectly conducting objects *J. Electromagn., Waves Appl.* **16** 771–91

[53] Tortel H 2004 Electromagnetic imaging of a three-dimensional perfect conducting object using a boundary integral formulation *Inverse Problems* **20** 385–98

[54] Vogel C R 2002 *Computational Methods for Inverse Pproblems (Frontiers in Applied Mathematics Series* vol 23*)* (Philadelphia, PA: SIAM)

[55] Yodh A G and Boas D A 2003 *Biomedical Photonics Handbook* (Boca Raton, FL: CRC Press)

[56] Zacharopoulos A, Arridge S, Dorn O, Kolehmainen V and Sikora J 2006 Shape reconstruction in optical tomography using spherical harmonics and BEM *PIERS 2006 Proc. (Cambridge, March 2006)* pp 48–52